# Part I
# Implementation and Technical Data

## 1. Modeling of fuel cell

### 1.1. Governing equations

For this model the current is split into an ionic and electronic part. Protons flow through the membrane and form an ionic current. The electrons only flow through the solid matrix of electrodes, resulting in an electronic current. Therefore, it satisfies the following proton potential equation [1]

$$\nabla \cdot (-\sigma_s \nabla \phi_s) = S_s \tag{1}$$

$$\nabla \cdot (-\sigma_m \nabla \phi_m) = S_m \tag{2}$$

where $\phi_s$ and $\phi_m$ are the protonic and electronic potential. The electronic conductivity is listed in Table 1, the protonic conductivity in electrolyte $\sigma_s$ is given by [1]

$$\sigma_s = \frac{1}{2} \left( 0.5139\lambda - 0.326 \right) \exp \left[ 1268 \left( \frac{1}{303} - \frac{1}{T} \right) \right] \tag{3}$$

and in porous electrode the protonic conductivity is

$$\sigma_{PE} = \varepsilon_{cm}^{1.5} \sigma_s. \tag{4}$$

$S$ is the current source term and defined as

anode catalyst layer:

$$S_m = j_a \quad S_s = -j_a \tag{5}$$

cathode catalyst layer:

$$S_m = j_c \quad S_s = -j_c \tag{6}$$

The source terms in both species and charge equations are related to the transfer current density $j_a$ and $j_c$, which was calculated by using a simplified Butler–Volmer equation given as

$$j_a = i_{0a} r_a \left( \frac{C_{H_2}}{C_{H_2,ref}} \right)^{0.5} \left( \frac{\alpha_a + \alpha_c}{RT} F \eta_a \right) \tag{7}$$

$$j_c = i_{0c} r_c \left( \frac{C_{O_2}}{C_{O_2,ref}} \right) \exp \left( -\frac{\alpha_c}{RT} F \eta_c \right) \tag{8}$$

1

where $\eta$ represents the potential difference between solid matrix and electrolyte and is defined as

anode side:

$$\eta_a = \phi_s - \phi_m \qquad (9)$$

cathode side:

$$\eta_c = \phi_s - \phi_m - V_{OC} \qquad (10)$$

*1.2. Fuel cell setup*

PEMFC consists of gas diffusion layers, porous electrode layers at anode and cathode side and the membrane in between [2].
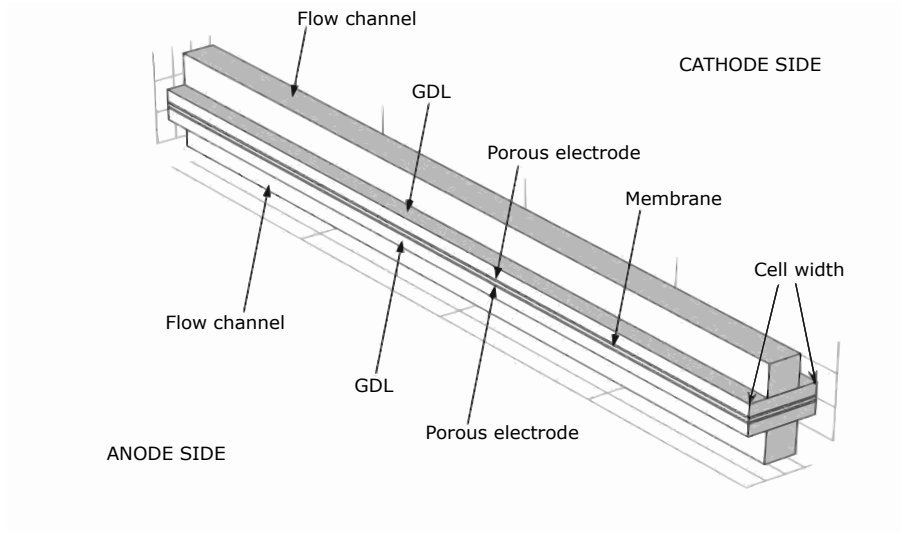


Figure 1: Geometry of the fuel cell model [2]

The coefficients are described in Table 1.

Table 1: Model parameters and values

| Parameter | Symbol | Value | Unit |
|-----------|--------|-------|------|
| Cell length | $L$ | $10^{-2}$ | m |
| Gas diffusion layers (GDL) thickness | $H_{gdl}$ | $38 \times 10^{-5}$ | m |
| Reference hydrogen molar concentration | $C_{\mathrm{H_2,ref}}$ | 40.88 | mol/m$^3$ |
| Reference oxygen molar concentration | $C_{\mathrm{O_2,ref}}$ | 40.88 | mol/m$^3$ |
| Electronic conductivity | $\sigma_m$ | 222 | S/m |
| Exchange current density, anode | $i_{0\mathrm{a}}$ | 1 | A/m$^2$ |
| Exchange current density, cathode | $i_{0\mathrm{c}}$ | 1 | A/m$^2$ |
| Ratio of reaction surface, anode | $r_{\mathrm{a}}$ | $10^9$ | 1/m |
| Ratio of reaction surface, cathode | $r_{\mathrm{c}}$ | $10^4$ | 1/m |
| Hydrogen concentrations | $C_{\mathrm{H_2}}$ | 60 | mol/m$^3$ |
| Oxygen concentrations | $C_{\mathrm{O_2}}$ | 10 | mol/m$^3$ |
| Transfer coefficient, anode | $\alpha_{\mathrm{a}}/\alpha_{\mathrm{c}}$ | 1/1 | - |
| Transfer coefficient, cathode | $\alpha_{\mathrm{c}}$ | 1 | - |
| Open circuit voltage | $V_{\mathrm{OC}}$ | 1.229 | V |
| Universal gas constant | $R$ | 8.31 | J/mol/K |
| Faraday constant | $F$ | 96485 | C/mol |
| | | | |
| Cell width | $W$ | $2 \times 10^{-3}$ | m |
| Membrane thickness | $H_{\mathrm{mem}}$ | $100 \times 10^{-6}$ | m |
| Porous electrode thickness | $H_{\mathrm{el}}$ | $50 \times 10^{-6}$ | m |
| Electrolyte phase volume fraction | $\varepsilon_{\mathrm{cm}}$ | 1 | - |
| Water content | $\lambda$ | 5 | - |
| Cell Temperature | $T$ | 453.15 | K |

*1.3. Variation of operation Fuel cell parameters*

The average cell power density is one of the most significant magnitudes of fuel cells whose increase is of paramount importance. The Fig. 2 shows the plot of average cell power density depending on the required voltage for different geometry parameters like cell width [$W$], membrane thickness [$H_{\mathrm{mem}}$] and porous electrode thickness [$H_{\mathrm{el}}$].
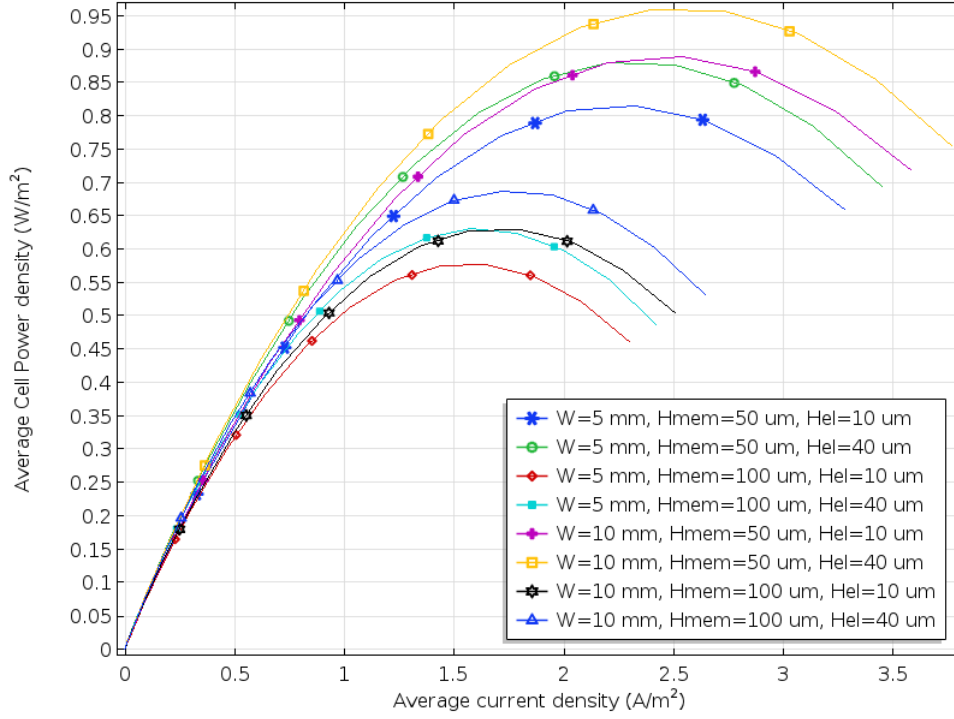
Figure 2: Variation of geometry parameters

The average cell power density is not only depended on cell geometry but also on other parameters listed in Table 1. In Fig 3 the average cell power density is plotted for other varying properties like hydrogen concentrations $[C_{H_2}]$, oxygen concentrations $[C_{O_2}]$ and the volume fraction of membrane in porous electrode $[\varepsilon_{cm}]$.
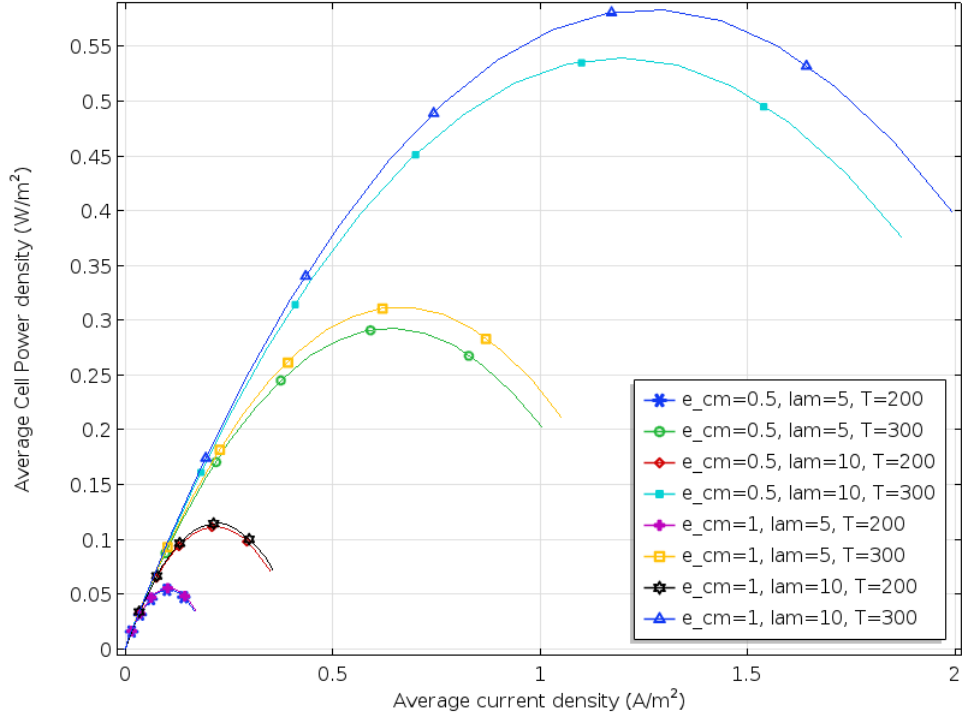
Figure 3: Variation of some other properties

The case is treated where a desired mean cell power density is given and the task is to find the parameters that achieve this power by variation. This is an optimization problem, and the genetic algorithm is used to solve the problem.

*1.4. Parameter identification through optimization*

In order to use a genetic algorithm, a solution space must first be specified. In our case, the following parameters are taken from Table 2 with a range and the step size is the resolution of the solution space.

Table 2: Solution space for genetic algorithms

| Symbol | Range | Step size | Unit |
|--------|-------|-----------|------|
| $W$ | $\begin{bmatrix} 1 & 10 \end{bmatrix}$ | 0.1 | mm |
| $H_{\mathrm{mem}}$ | $\begin{bmatrix} 10 & 110 \end{bmatrix}$ | 10 | $\mu$m |
| $H_{\mathrm{el}}$ | $\begin{bmatrix} 10 & 110 \end{bmatrix}$ | 1 | $\mu$m |
| $\varepsilon_{\mathrm{cm}}$ | $\begin{bmatrix} 0.1 & 1 \end{bmatrix}$ | 0.1 | - |
| $\lambda$ | $\begin{bmatrix} 1.5 & 15 \end{bmatrix}$ | 1.5 | - |
| $T$ | $\begin{bmatrix} 200 & 400 \end{bmatrix}$ | 20 | K |

5

From the solution space an initial population is randomly generated which is a set of individuals or chromosomes. The position or locations in a chromosome are referred to as genes to which individual parameters are assigned.

Since the fitness function is a positive real number, it is obtained by scaling from the objective function, which corresponds to the optimization goal of the optimization problem. The objective function that is used is the average cell power density

$$F_p = \sqrt{\sum_{i=1}^{N} |p_i \left(W, H_{\text{mem}}, ..., T\right) - \hat{p}_i|^2} \rightarrow \min \tag{11}$$

where $p_j$ is the simulated and $\hat{p}_j$ the desired average cell power density. Index $j$ represents various points on the average cell power density curve where the simulated and desired average cell power density are compared and evaluated. The number of points is chosen as N = 21 that means that the output power is evaluated for 21 different required output voltages. .

## 2. Modeling of reverberation chamber

### 2.1. Governing equations

A real life ERC differs from a cavity resonator because it normally contains one or more stirrers [3]. However, due to the simplicity of the model, it is still preferable to start by analyzing a cavity resonator and later supplement the model in order to achieve an ERC. Thus, the Helmolz equation is initially applied to the electric and magnetic fields of the cavity resonator through

$$\triangle \vec{E}(\vec{r}) + k^2 \cdot \vec{E}(\vec{r}) = 0 \tag{12}$$

$$\triangle \vec{H}(\vec{r}) + k^2 \cdot \vec{H}(\vec{r}) = 0 \tag{13}$$

$$k = \frac{\omega}{\sqrt{\varepsilon_0 \mu_0}} \tag{14}$$

where $\varepsilon_0$ the permittivity and $\mu_0$ the permeability of the medium (air) is in which the wave is propagating. Due to their almost equal qualities, the permittivity and the permeability for the vacuum will be used instead of those for air. In addition, it is assumed that the tangential components of the electric field and the normal components of the magnetic field on the walls disappear as seen in

$$\vec{n} \times \vec{E} = 0 \tag{15}$$

$$\vec{n} \cdot \vec{H} = 0 \tag{16}$$

where $\overrightarrow{n}$ is the surface normal vector and the convention is also used that the z-axis is chosen as the reference direction. This leads to the discrete solution in the direction of the z-axis for the electric and magnetic fields with the resonance frequency

$$f_{res} = \frac{1}{2}\frac{1}{\sqrt{\varepsilon_0\mu_0}}k_{xyz} = \frac{1}{2}\frac{1}{\sqrt{\varepsilon_0\mu_0}}\sqrt{\left(\frac{l}{a}\right)^2 + \left(\frac{m}{b}\right)^2 + \left(\frac{n}{c}\right)^2} \tag{17}$$

for the number triple $l, m$ and $n$ applies, $l, m = 0, 1, 2, 3...$ and $n = 1, 2, 3....$

### 2.2. Reverberation chamber Setup

An overview of the setup of the aluminium resonance chamber was modeled and is displayed in Fig.4. A mode stirrer and a Vivaldi antenna - as a transmitting antenna exciting the field inside the ERC - were placed inside the chamber. The details describing the geometry and position for each item are listed in Table 3.
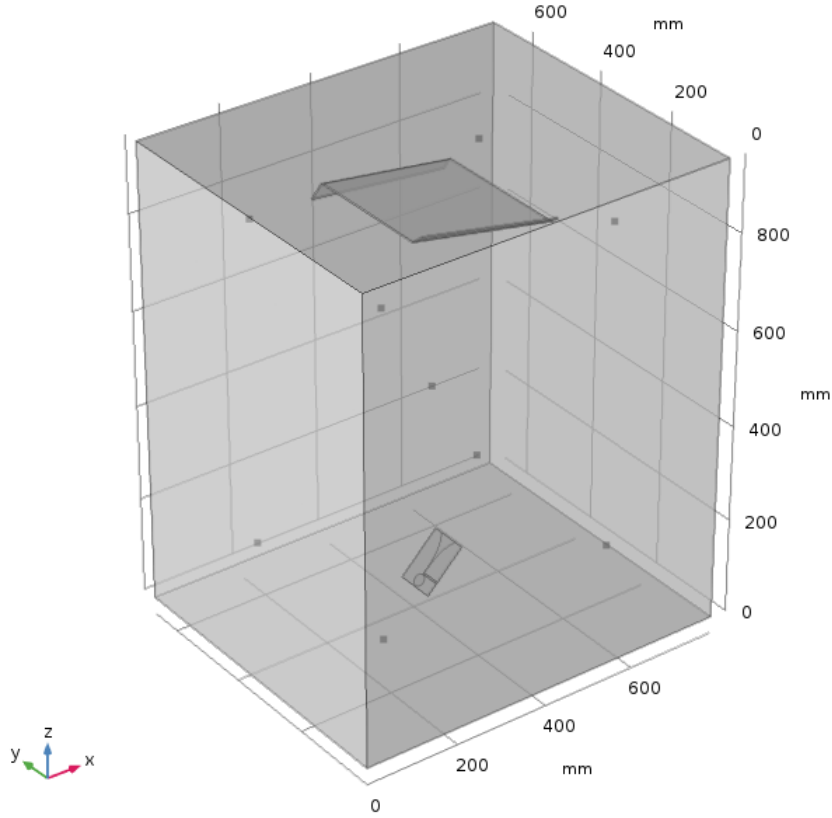


Figure 4: Geometry of the resonance chamber, see Table 3 for details

A Vivaldi antenna was chosen as the source for the simulation due to the wideband characteristic. As shown in Fig.5, the antenna was positioned in the center of the xy-plane of the chamber floor with an established angle and height from the chambers floor.
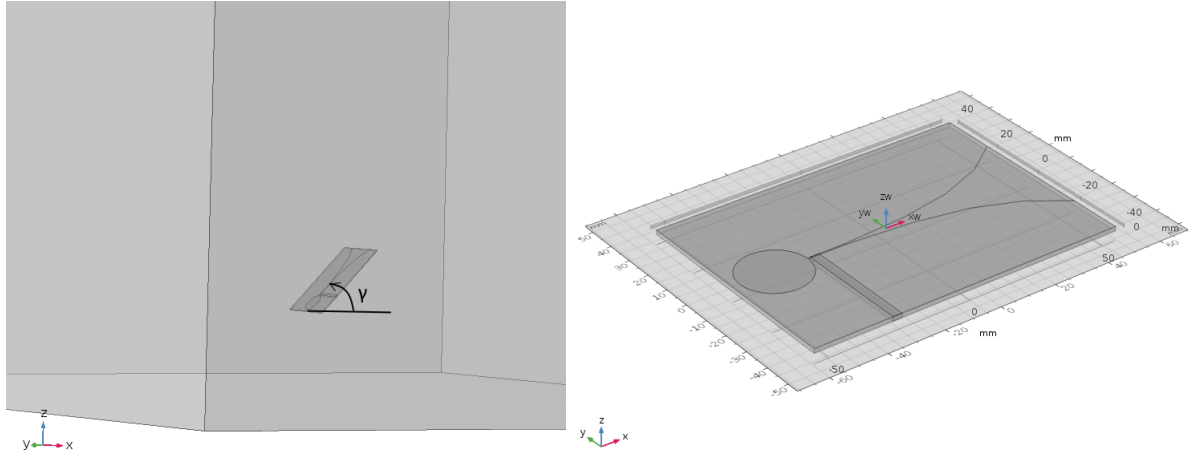
Figure 5: Vivaldi antenna geometry and position, see Table 3

Fig.6 shows a close up view of the stirrer and specifies the angle of the stirrer wings, the distances of the wings, and the length and width of the stirrer. Significant parameters this work will be concerned with are distances $tr_1y_1$, $tr_1y_2$, $tr_2y_1$, and $tr_2y_2$ which correspond to the distance of the wing edges from the boundary of the stirrer length $St_L$.
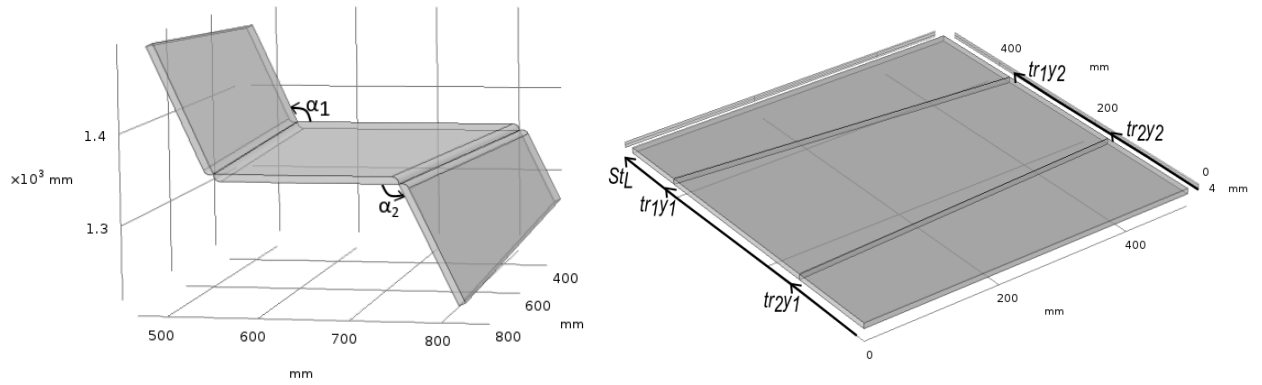


Figure 6: Stirrer geometry and angle of wings

All the parameters and the designated values that are represented in the figures shown above have been described in Table 3.

Table 3: Model parameters and values

| Equipment | Parameter | Symbol | Value | Unit |
|---|---|---|---|---|
| Aluminum Chamber | Height | $Ch_H$ | 960 | mm |
| | Width | $Ch_W$ | 790 | mm |
| | Length | $Ch_L$ | 673 | mm |
| | | | | |
| Vivaldi Antenna | Height | $An_H$ | 80 | mm |
| | Length | $An_L$ | 110 | mm |
| | Thickness | $An_{Th}$ | 1.5 | mm |
| | Angle in chamber | $\gamma$ | 45 | degree |
| | Position in x-direction | $An_{x,\text{pos}}$ | 0 | mm |
| | Position in y-direction n | $An_{y,\text{pos}}$ | 0 | mm |
| | Position in z-direction | $An_{z,\text{pos}}$ | 100 | mm |
| | Frequency | $f$ | 2.1603 | $\text{GH}_z$ |
| | Characteristic impedance | $Z_{ref}$ | 50 | $\Omega$ |
| | Voltage | $V_0$ | 7 | V |
| | Substrate thickness | $H$ | 1.6 | mm |
| | | | | |
| Stirrer | Length | $St_L$ | 340 | mm |
| | Width | $St_W$ | 300 | mm |
| | Thickness | $St_{Th}$ | 3 | mm |
| | Position in x direction | $St_{x,\text{pos}}$ | 0 | mm |
| | Position in y direction | $St_{y,\text{pos}}$ | 0 | mm |
| | Position in z direction | $St_{z,\text{pos}}$ | 860 | mm |
| | Angle of stirrer wings | $\alpha_1$ | 60 | degree |
| | Angle of stirrer wings | $\alpha_2$ | 40 | degree |
| | Angle in relation to ceiling | $\beta$ | 10 | degree |
| | Distance 1 | $tr_1y_1$ | 240 | mm |
| | Distance 2 | $tr_1y_2$ | 100 | mm |
| | Distance 3 | $tr_2y_1$ | 240 | mm |
| | Distance 4 | $tr_2y_2$ | 100 | mm |

*2.3. Variation of the stirrer shape and quantity in an ERC*

*2.3.1. Simulation Performance*

As mentioned in the previous chapter, both the shape and the number of stirrers are crucial to achieve a statistically uniform and isotropic field. First, the shape of a stirrer is considered and changed. To do this, all parameters in the table 3 are left at the same value except for the four distance. These values change the shape of the wings. The model was simulated for 40 stirrer positions and 9 degree steps and measurements were recorded from 9 different points spaced out within the chamber. From these points a value of the electric

field in both imaginary and rael parts in each direction was measured and averaged over 9 points. The following distribution of these fields is displayed for distance in table 3.
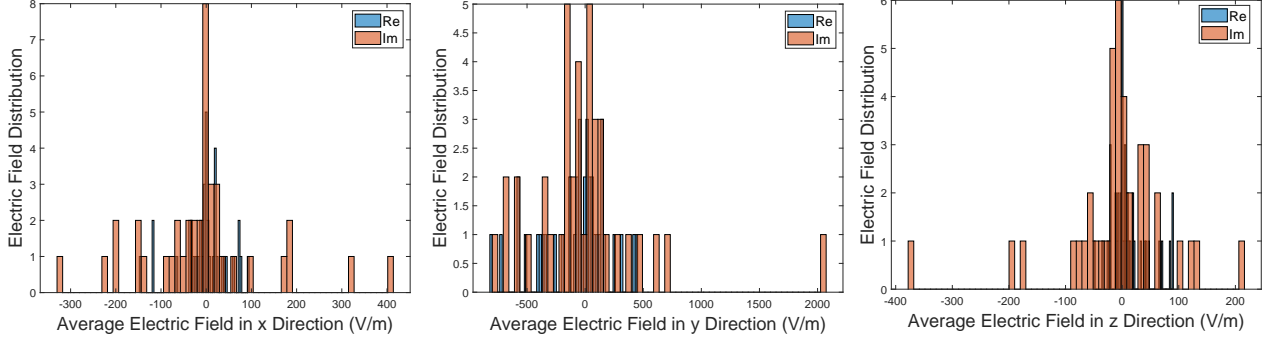


Figure 7: Distribution of the average electric field

Resulting from these electric field distributions, the following $P$-values were determined in Matlab.

Table 4: Resulting $P$-values of the simulation

| Average Electric Field Distribution | Direction | $P$-value | $\sigma$ in V/m |
|---|---|---|---|
| Real Part | $x$ | 0.0078 | $48, 75$ |
| | $y$ | 0.0505 | $296, 54$ |
| | $z$ | 0.0036 | $34, 25$ |
| | | | |
| Imaginary Part | $x$ | 0.0030 | $133, 67$ |
| | $y$ | $2.3123 \times 10^{-5}$ | $464, 76$ |
| | $z$ | $1.0217 \times 10^{-4}$ | $92, 64$ |

The $P$-values from the simulation with the initial stirrer geometry do not reach the requirements discussed in the previous chapter. Consequently, these results lead to the construction of a new stirrer whose geometry allows for higher $P$-values. Thus, this issue will be considered as an optimization problem, that will be solved through the use of genetic algorithms.

### 2.3.2. Performance of the optimized stirrer geometry

The following parameters listed in Table 5 are the solution spaces for the algorthms, where the range and step size build the resolution of this space.

Table 5: Solution space for genetic algorithms

| Symbol | Range | | Step size | Unit | Description |
|--------|-------|---|-----------|------|-------------|
| $tr_1y_1$ | 240 | 330 | 9 | mm | distance |
| $tr_1y_2$ | 240 | 330 | 9 | mm | distance |
| $tr_2y_1$ | 10 | 100 | 9 | mm | distance |
| $tr_2y_2$ | 10 | 100 | 9 | mm | distance |

The objective function that we used is the Shapiro-Wilk-Test value $P$ for the real and imaginary average electric field in each of the three directions in terms of the different parameters or distance.

$$F_P = \sqrt{\sum_{i=1}^{6} |P_i\left(tr_1y_1, tr_1y_2, tr_2y_1, tr_2y_2\right) - 1|^2} \to \min. \tag{18}$$

*2.3.3. Performance of the optimized shape for three stirrers in chamber*
In Fig.8, we observe the reverberation chamber with three stirrer whose geometries have will later be optimized.
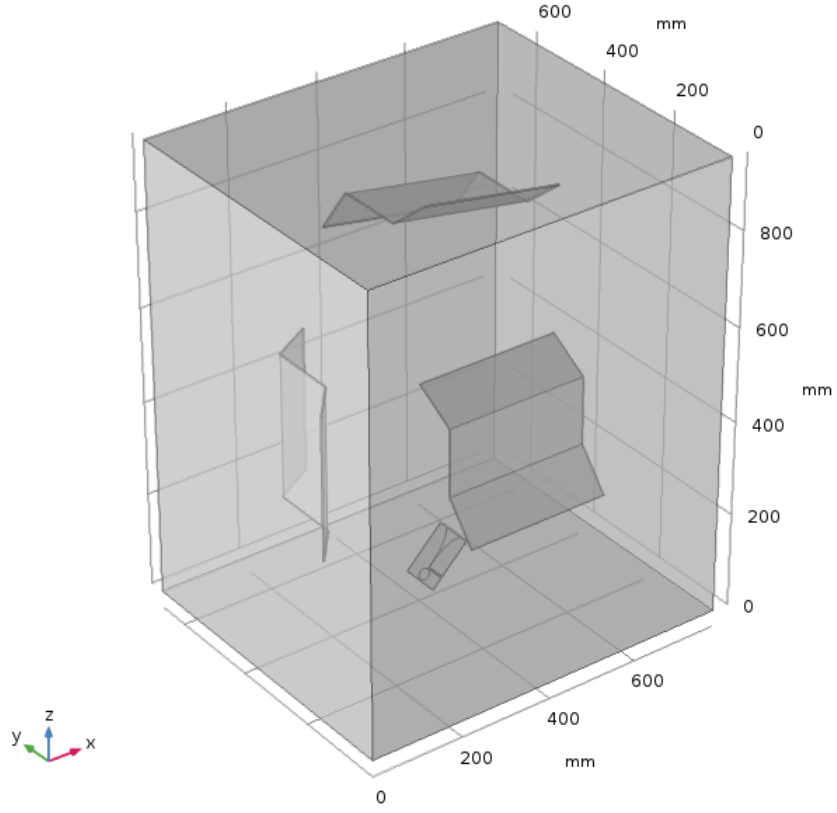
Figure 8: Setup of the resonance chamber with three stirrers, see Table 6 for their postions

The positions of all three stirrers are listed in Table 6.

Table 6: Model parameters and values

| Equipment | Parameter | Symbol | Value | Unit |
|-----------|-----------|--------|-------|------|
| Stirrer 1 | Position in x direction | $St_{x,1}$ | 0 | mm |
|           | Position in y direction | $St_{y,1}$ | 0 | mm |
|           | Position in z direction | $St_{z,1}$ | 860 | mm |
| Stirrer 2 | Position in x direction | $St_{x,2}$ | 0 | mm |
|           | Position in y direction | $St_{y,2}$ | 100 | mm |
|           | Position in z direction | $St_{z,2}$ | 0 | mm |
| Stirrer 3 | Position in x direction | $St_{x,3}$ | 100 | mm |
|           | Position in y direction | $St_{y,3}$ | 0 | mm |
|           | Position in z direction | $St_{z,3}$ | 0 | mm |

The parameters that have been chosen to be optimized are the shape of the wings for all

12

three stirrers inside the chamber. The newly formulated fitness function for these selected parameters is

$$F_P = \sqrt{\sum_{i=1}^{6} |P_i\left(tr_{11}y_1, ..., tr_{23}y_2\right) - 1|^2} \rightarrow \min. \tag{19}$$

A new solution space for the three stirrers is specified in Table 7.

Table 7: Solution space for genetic algorithms

| Equipment | Symbol | Range | | Step size | Unit | Description |
|-----------|--------|-------|-------|-----------|------|-------------|
| Stirrer 1 | $tr_{11}y_1$ | 240 | 330 | 9 | mm | stirrer wing distance 1 |
|           | $tr_{11}y_2$ | 240 | 330 | 9 | mm | stirrer wing distance 2 |
|           | $tr_{21}y_1$ | 10 | 100 | 9 | mm | stirrer wing distance 3 |
|           | $tr_{21}y_2$ | 10 | 100 | 9 | mm | stirrer wing distance 4 |
| Stirrer 2 | $tr_{12}y_1$ | 240 | 330 | 9 | mm | stirrer wing distance 1 |
|           | $tr_{12}y_2$ | 240 | 330 | 9 | mm | stirrer wing distance 2 |
|           | $tr_{22}y_1$ | 10 | 100 | 9 | mm | stirrer wing distance 3 |
|           | $tr_{22}y_2$ | 10 | 100 | 9 | mm | stirrer wing distance 4 |
| Stirrer 3 | $tr_{13}y_1$ | 240 | 330 | 9 | mm | stirrer wing distance 1 |
|           | $tr_{13}y_2$ | 240 | 330 | 9 | mm | stirrer wing distance 2 |
|           | $tr_{23}y_1$ | 10 | 100 | 9 | mm | stirrer wing distance 3 |
|           | $tr_{23}y_2$ | 10 | 100 | 9 | mm | stirrer wing distance 4 |

*2.4. Variation of geometrie and amount of built-in objects in an ERC*

*2.4.1. Simulation of using different geometric objects in ERC*

Arrays of the chosen two geometric objects, half spheres and cones, were inserted inside the chamber cavity 9 with parameters specified in Table 8. These equidistant objects are of the same radius (R= 120 mm) and are modeled as such in order to ultimately compare the values of each simulation and, thus, posses the representation with the better results.
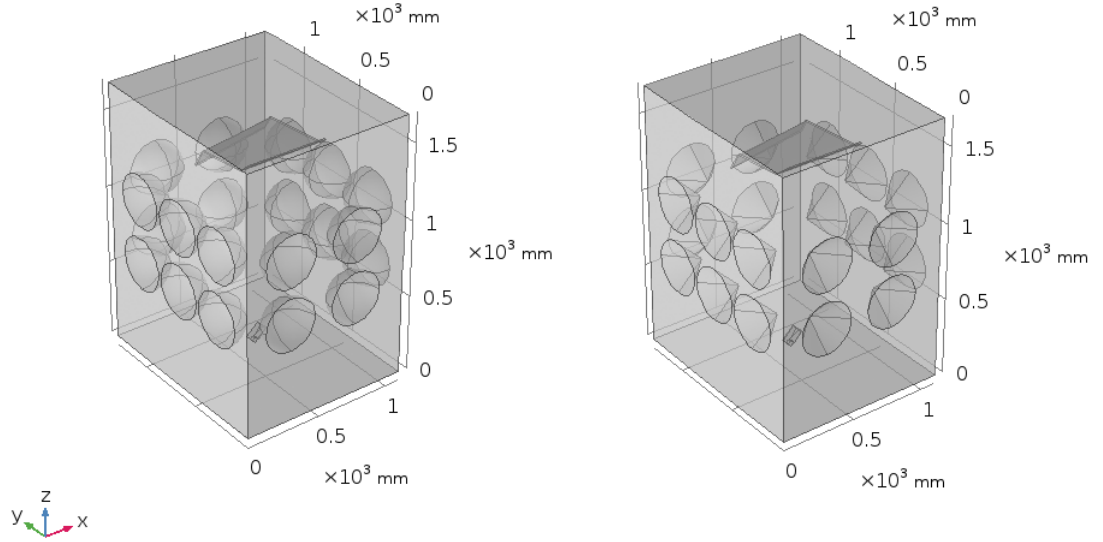
Figure 9: Electromagnetic resonance chamber with half spheres and cones plaiced inside with the same distance between each other

The dimensions of the chosen objects, as seen in Table 8, were similarly selected in order to definitively say which geometry produces more satisfactory results.

Table 8: Dimensions of used geometric objects

| Symbol | Optimized Values | Unit | Description |
|---|---|---|---|
| $Rad_{Sph}$ | 120 | mm | radius of the sphere |
| $Rad_{Con}$ | 120 | mm | radius of the cone |
| $Con_H$ | 120 | mm | cone height |

Following several simulations and evaluations, the subsequent distributions of the average electric field for both geometries were produced. Fig. 10 represent the electric field distribution for the model with half spheres in all three directions.
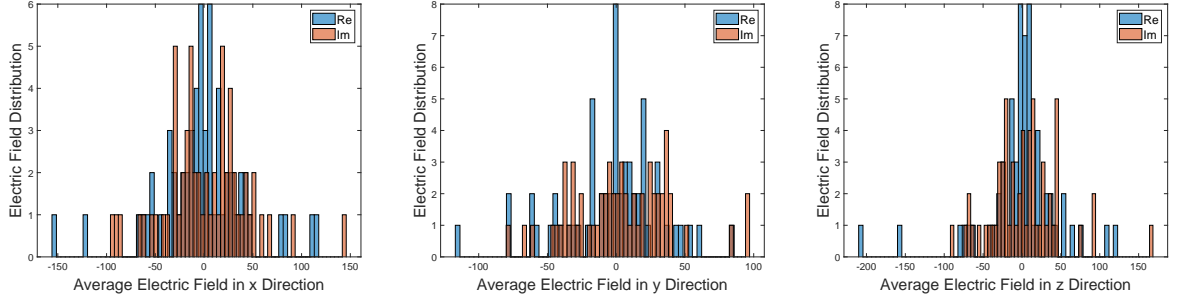
14

Figure 10: Distribution of the average electric field for half spheres

Subsequently, the electric field distribution for the reverberation chamber with the cones was simulated and represented in Fig. 11. This distribution is, as well, shown for all three directions and for both real and imaginary part. All figures already serve to portray the difference between the two models. At first sight, one can so far determine that the distribution observed for figures relating to the half spheres end up fulfilling expectations more so than those of the cones. These observations are further proven true in Table 9.
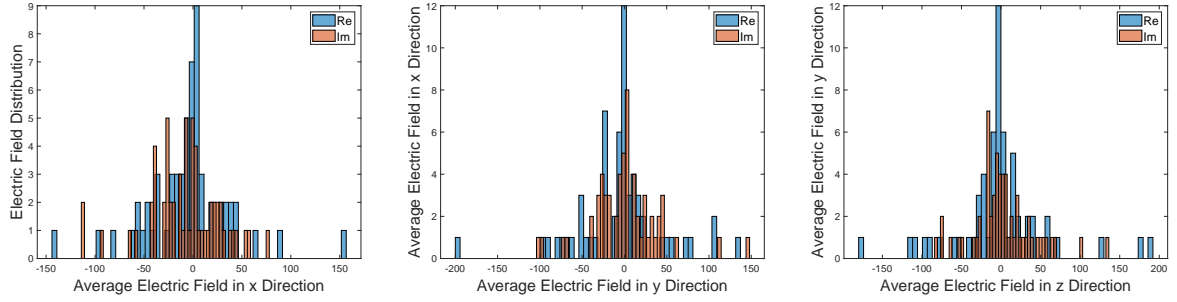


Figure 11: Distribution of the average electric field for cones

The resulting P-values achieved by both models are listed below in Table 9 and given for both real and imaginary parts of the field.

Table 9: Resulting P-values of the simulation

| Average Electric Field Distribution | Direction | P-value of Half Sphere | P-value of Cone |
| --- | --- | --- | --- |
| Real Part | $x$ | 0.0024 | $3.4875 \times 10^{-4}$ |
| | $y$ | 0.0513 | $2.6074 \times 10^{-4}$ |
| | $z$ | $6.2473 \times 10^{-6}$ | $2.7340 \times 10^{-5}$ |
| | | | |
| Imaginary Part | $x$ | 0.0893 | 0.0294 |
| | $y$ | 0.2413 | $9.0150 \times 10^{-4}$ |
| | $z$ | 0.0095 | 0.0085 |

The P-values serve to emphasize the contrast of both geometries and, thus, help in the choice of a better suited geometry for the ERC. The P-values calculated for the half spheres are remarkably better than those of the cones as half of them succeed the previously established desired goal of at least 5%, whereas none of the values of the cone simulation come even close to approaching the needed standard. Nevertheless, the P-values are still not perfect and need to be optimized further.

## References

[1] HE, Mingyan ; HUANG, Ziping ; SUN, Pengtao ; WANG, Cheng: Modeling and Numerical Studies for a 3D Two-Phase Mixed-Domain Model of PEM Fuel Cell. In: *Journal of The Electrochemical Society* 160 (2013), Nr. 4. `http://dx.doi.org/10.1149/2.036304jes`. – DOI 10.1149/2.036304jes

[2] UBONG, E. U. ; SHI, Z. ; WANG, X.: Three-Dimensional Modeling and Experimental Study of a High Temperature PBI-Based PEM Fuel Cell. In: *Journal of The Electrochemical Society* 156 (2009), Nr. 10, B1276. `http://dx.doi.org/10.1149/1.3203309`. – DOI 10.1149/1.3203309

[3] KRAUTHÄUSER, Hans G.: *Grundlagen und Anwendungen von Modenverwirbelungskammern.* `http://dx.doi.org/10.25673/4794`. Version: 2007